RSC Advances

PAPER

View Article Online
View Journal | View Issue

Published on 27 January 2016. Downloaded by Synchrotron Radiation Library on 23/11/2016 03:11:24.

Cite this: *RSC Adv.*, 2016, **6**, 13185

Electrochemically fabricated gold dendrites with underpotential deposited silver monolayers for a bimetallic SERS-active substrate†

Ying-Huang Lai,*[a] Shan-Chi Kuo,[a] Yun-Ching Hsieh,[b] Yu-Chun Tai,[a] Wei-Hsiu Hung*[b] and U-Ser Jeng*[cd]

Received 17th December 2015
Accepted 25th January 2016

DOI: 10.1039/c5ra27020k

www.rsc.org/advances

With electrochemical deposition, cysteine-directed crystalline gold dendrites (Au-Ds) on glassy carbon electrodes were fabricated. The Au-Ds surfaces were further modified with Ag adatoms by underpotential deposition (UPD) for Ag-covered Au-Ds (Ag–Au-Ds). The Ag–Au-Ds possessed a hierarchical architecture comprising trunks, branches, and nanoleaves for a threefold-symmetry, resulting in a high density of sharp tips and edges for hot spots of surface-enhanced Raman scattering (SERS). Prominent SERS was observed with *p*-nitrothiophenol (*p*-NTP) adsorption onto either Au-Ds or Ag–Au-Ds, for a best *p*-NTP detection limit down to 5–10 nM at 785 nm laser excitation. However, at specific 633 nm laser excitation, SERS with *p*-NTP adsorption on Ag–Au-Ds exhibited a three-fold higher enhancement over that measured for *p*-NTP adsorbed on unmodified Au-Ds, suggesting an increased chemical SERS enhancement with the Ag–*p*-NTP bonding. Furthermore, adsorption isotherms of *p*-NTP with Au-Ds and Ag–Au-Ds adsorption in solution are established from solution *p*-NTP-concentration dependent SERS; from which, comparable binding constants of *p*-NTP to Au-Ds and Ag–Au-Ds are extracted.

Introduction

Surface-enhanced Raman scattering (SERS) has widespread application in various fields, for example, molecular sensing, DNA or/and RNA detection, and advanced materials research.[1–4] Two commonly accepted mechanisms of SERS enhancement are the electromagnetic mechanism (EM) and the chemical mechanism (CM).[5] EM involves enhanced E-field intensity due to excitation of surface plasmons of the metal colloidal or roughened metal surfaces, hence significantly increased SERS intensity of the absorbed molecules. The enhancement *via* EM is roughly proportional to the fourth power of the E-field. In contrast, CM enhances SERS by one to two order-of-magnitude *via* increased polarizability from charge transfer between the adsorbed molecule and the substrate. Among the most studied SERS materials, arrays of metal nanoparticles show impressive SERS enhancements based on EM;[6,7] whereas graphene substrates illustrate much improved SERS based on CM.[8]

Development of nanostructured substrates for highly reproducible and efficient SERS enhancement is one of the most active areas in SERS research.[4,7,8] The SERS-active substrates of surface plasmon resonances from the nanostructures can efficiently collect and amply, like an antenna, incident and scattered E-fields near the nanostructured metal surfaces. The scattered light can be further modulated, from site to site, by featured resonant frequencies relevant to the architecture of the adsorbed molecules and their bonding to the metal surfaces.[6,9] Currently, the most commonly used SERS-active materials are silver, gold, and copper. With colloidal or roughened surfaces of nano-structural features, these metal surfaces possess rich surface plasmon resonances upon E-wave excitation.[10,11] Particularly, SERS-active substrates of a high density of hot spots can provide impressive enhancement factors (EF) of SERS intensity, allowing detection of target molecules in very low concentrations.

Numerous designs of two-dimensional (2D) SERS substrates such as arrays of metallic nanostructured objects or surfaces have been proposed for their high densities of hot spots of SERS. However, 2D SERS substrates are limited by the surface areas available.[7,12] Alternatively, three-dimensional (3D) nanodendritic materials with rich surface areas, tips, edges, and junction positions, can provide a highly elevated density of SERS hot spots.[13–15] Many approaches were hence developed to

[a]*Department of Chemistry, Tunghai University, Taichung 40704, Taiwan. E-mail: yhlai@go.thu.edu.tw; Fax: +886 4 23590426; Tel: +886 4 23590121 ext. 32216*

[b]*Department of Chemistry, National Taiwan Normal University, Taipei 11677, Taiwan. E-mail: whung@ntnu.edu.tw*

[c]*National Synchrotron Radiation Research Center, Hsinchu 30076, Taiwan. E-mail: usjeng@nsrrc.org.tw*

[d]*Chemical Engineering Department, National Tsing-Hua University, Hsinchu, 30013, Taiwan*

† Electronic supplementary information (ESI) available. See DOI: 10.1039/c5ra27020k

Published on 27 January 2016. Downloaded by Synchrotron Radiation Library on 23/11/2016 03:11:24.

prepare dendritic noble metals, including galvanic replacement, electrochemical techniques, seeding, and displacement reactions.[16–18] Among them, conventional electrochemical techniques provide reliable and robust routes for preparation of 3D metallic dendrites. Recently, the formation of gold dendrites (Au-Ds) *via* electrochemical deposition using cysteine as a directing agent for dendrite structures was reported.[19] The rich and open 3D nanostructures for vast surface area and the corresponding wide-range surface plasmon resonances, together with easy fabrication and chemical stability, make Au-Ds promising SERS-active substrates for detections of organic analytes. Very efficient SERS-active sites of such Au-Ds hence observed were originated from EM.[20,21] On the basis of the 3D Au-Ds, also developed were silver-modified gold substrates of improved SERS based on enriched spectra of surface plasmon resonances from the bimetallic SERS substrates.[22,23]

In this study, we propose an electrochemical pathway to prepare Au-Ds on glassy carbon electrode (GCE), with the Au surfaces further modified by Ag adatoms using underpotential deposition (UPD)[11,24,25] for monolayer-Ag deposition on Au-Ds (Ag–Au-Ds). We show that the hence fabricated 3D SERS substrates have selectively enhanced CM-based SERS due to the Ag–analyte bonding, in addition to the same EM-based SERS from the underlying Au-Ds. Furthermore, we have investigated the sensing capability of Au-Ds and Ag–Au-Ds to *p*-nitrothiophenol (*p*-NTP) in solution, *via* SERS with 532, 633, and 785 nm laser excitations. The Ag–Au-Ds/GCE demonstrates a detecting limit of 5–10 nM of *p*-NTP and a relatively enhanced SERS at specific 633 nm laser excitation, compared to that of the Au-Ds/GCE.

Experimental

Materials

Hydrogen tetrachloroaurate trihydrate ($HAuCl_4 \cdot 3H_2O$, Acros, ACS analytical grade), *p*-NTP, and cysteine (Acros, >99%) were used without further purification. GCE was employed as a deposition substrate for surface characterization of the electrodeposited Au. Before deposition, the GCE surface was sequentially polished with two alumina slurries (0.3 and 0.05 μm) by using a nanocloth. The polished GCE was further cleaned in an ultrasonic water bath with ethanol for 15 min, and then thoroughly rinsed with ultrapure water.

Preparation of Au-Ds/GCE

Au-Ds were prepared by a synthesis route modified from that reported previously.[19] Au was electrochemically deposited on GCE in an aqueous solution containing 1.0×10^{-3} M $HAuCl_4$, 0.5 M H_2SO_4, and 1.0×10^{-4} M cysteine. The Au dendrites were formed at cysteine concentrations of $<1.0 \times 10^{-3}$ M because the growth of Au crystals could be confined to the ⟨111⟩ direction; crystal growth in all crystallographic facets would be severely inhibited at higher concentrations of cysteine. A conventional three-electrode system in an electrochemical workstation (CHI 614B) was employed for electrodeposition, with a saturated calomel electrode (SCE) served as a reference electrode and a platinum wire as the counter electrode. Square-wave potential pulses were applied to the GCE at a frequency of 5 s^{-1} for 3000 s. A pulsed potential form was used to reduce the effect of diffusion limits on the electrodeposition rate. Low and high potential limits of the square-wave pulse with respect to the SCE were set to −0.8 and +0.2 V, respectively.

Au-Ds modified by monolayer-Ag coverage (Ag–Au-Ds)

Silver atoms were electrodeposited on the Au-Ds surfaces at 24 mV in the underpotential deposition regime to form monolayers on the gold surfaces.[11] Soon after the deposition, the Ag–Au-Ds/GCE was retrieved and rinsed with distilled water, then dried in a nitrogen atmosphere for 30 min at ambient temperature.

Material characterization

Powder X-ray diffraction (PXRD). PXRD measurements at an X-ray wavelength of 0.775 Å were performed at the BL01C2 PXRD end-station of the National Synchrotron Radiation Research Center (NSRRC) in Taiwan.[26] PXRD data were collected with an image plate (Mar 345), and the diffraction angle 2θ was calibrated by using diffractions from powder mixtures of silicon and silver behenate.

Scanning electron microscopy (SEM). Field emission SEM measurements were made under a JEOL JSM-6700F microscope operated at an acceleration voltage on 3.0 kV.

X-Ray photoemission spectroscopy (XPS) measurements. The chemical constituents of Au-Ds and Ag–Au-Ds electrodeposited on GCE surfaces were revealed from the XPS spectra measured at the scanning photoelectron microscopy end station of the NSRRC beamline 09A1. The onset of photoemission from an Au foil attached to the sample holder was used to calibrate the Fermi level as the zero binding energy;[27] Au 4f and Ag 3d XPS spectra of the Au-Ds/GCE and Ag–Au-Ds/GCE were obtained with an incident beam of an X-ray energy 620 eV.

Electrochemical surface area (ESA) measurements. The surface areas of Au-Ds were deduced from cyclic voltammetry (CV) scans with the Au-Ds/GCE soaked in a N_2-saturated H_2SO_4 solution (0.50 M) at a scan rate of 50 mV s^{-1}. Cyclic voltammograms were recorded between 0.12 and 1.32 V *versus* SCE at room temperature. The ESA of Au-Ds/GCE was estimated by coulombic integration of the enhanced cathodic peak current at 0.79 V, as detailed in ESI.†

SERS measurements. SERS samples were prepared by immersing the Au-Ds/GCE or Au–Ag-Ds/GCE in a 1 mL ethanol solutions containing specified concentrations (1.0 nM to 1.0 mM) of *p*-NTP for 20 min for the chemical adsorption at room temperature. The samples were then rinsed with ethanol to remove excess *p*-NTP and finally dried under ambient conditions. Raman scattering spectra were recorded using a micro-Raman system detailed in our previous report.[28] Samples with 1 μm diameter were respectively irradiated with laser beams of wavelengths 532 nm (16 mW), 632.8 nm (35 mW), and 785 nm (5.1 mW), with 40×/0.65 N.A. objective lens (Plan N, Olympus). The 1001.4 cm^{-1} Raman band of a polystyrene plate was used to calibrate the spectra. The laser exposure time for each scan was

 This journal is © The Royal Society of Chemistry 2016

Published on 27 January 2016. Downloaded by Synchrotron Radiation Library on 23/11/2016 03:11:24.

10 s; six scans were averaged for each final spectrum to improve data statistics.

Results and discussion

Fig. 1(a) shows a typical low-magnification SEM image of the Au-Ds/GCE, revealing a hierarchical architecture comprising trunks, branches, and nanoleaves in a threefold-symmetry. A zoom-in (Fig. 1(b)) of the SEM image illustrates a high density of sharp tips and edges that are advantages for serving as hot spots of SERS. The SEM images show that the Au-Ds cover a wide length scale from nanometers to micrometers and are rich in roughened surfaces and branches that are oriented radially away from the main stem; numerous secondary structures of leave-like morphology are densely populated along each branch, with a regular include angle *ca.* 68° between each stem and the leaves.[19] Furthermore, the SEM image of the Au-Ds modified by UPD Ag in Fig. 1(c) shows a similar hierarchical structure as that observed for Au-Ds. The high-magnification SEM image of the Ag–Au-Ds/GCE (Fig. 1(d)) further illustrated similar nanostructural details as that of Au-Ds. There are, however, no observable thick layers or aggregates of Ag. The result suggests that the UPD Ag atoms formed largely thin- or mono-layers of Ag on the gold surfaces of Au-Ds, without altering much the nano structural features of Au-Ds.

The existence of Ag adatoms on the Au-Ds surfaces was confirmed by surface composition analysis using XPS. As shown in Fig. 2(a), signals of Au-Ds at binding energies of *ca.* 285 and 86 eV appeared after reductive desorption of cysteine, indicating respectively C 1s and Au 4f electron energy levels. In contrast, the XPS spectrum for Ag–Au-Ds revealed the Ag MNN Auger and Ag 3d signals in Fig. 2(c), in additional to the prominent Au 4f peak, suggestion existing of Ag adatoms on the gold surfaces of the Ag–Au-Ds. High-resolution XPS measurements were carried out to examine the electronic states of Au and Ag on the dendrites. Fig. 2(b) and (d) shows the Au 4f core-level spectra obtained before and after modification with UPD Ag. Both Au 4f spectra can be fitted with a pair of doublet peaks of the binding energy at 84.0 and 87.7 eV, respectively corresponding to $4f_{7/2}$ and $4f_{5/2}$ levels of metallic Au atoms. Moreover, the Au 4f peak intensities measured after modification with UPD Ag adatoms were attenuated marginally only by *ca.* 15% of that of Au-Ds, suggesting that the Au-Ds surface area was largely covered by Ag monolayers. Correspondingly, the Ag 3d core-level spectrum of the Ag–Au-Ds shown in Fig. 2(e) can be fitted with a pair of doublet peaks at 367.8 and 373.8 eV, respectively corresponding to $3d_{5/2}$ and $3d_{3/2}$ energy levels of Ag atoms. We note that the peak position of Ag $3d_{5/2}$ located at 367.8 eV is negatively shifted by 0.2 eV with respect to that of bulk Ag, and is nearly identical with the reported 367.88 eV for the Ag atoms adsorbed on Au (111) in the form of sub-monolayer or monolayer structure.[29]

Shown in Fig. 3 are similar PXRD patterns of Au-Ds and the Ag-covered Au-Ds dendrites, indicating a same crystalline structure. These observed sharp diffraction peaks are consistent with (111), (200), (220), (311), and (222) reflections of the well-known face-centered cubic (fcc) lattice structure of gold crystals. In addition, the intensity ratios the (200) and (220) peak intensities normalized by that of (111) peak intensity, *ca.* 0.33 and 0.2, suggest a preferred crystal growth direction along (111),

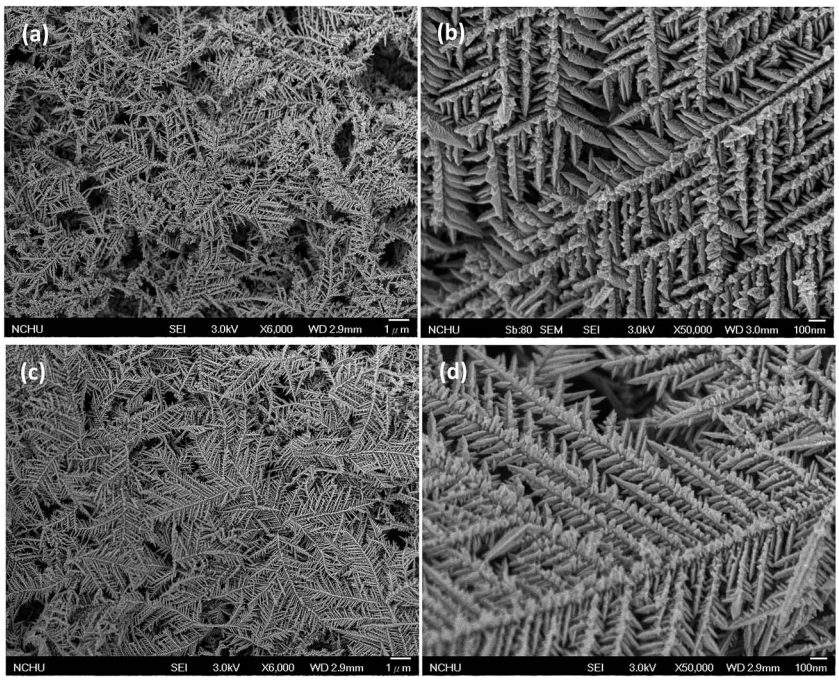

Fig. 1 (a) Representative SEM image of Au-Ds on GCE, and (b) the corresponding room-in image, as marked by the length scale bar. (c) and (d) are the corresponding SEM images for Ag–Au-Ds on GCE. The samples were prepared in a 0.5 M H_2SO_4 solution containing 1.0 mM $HAuCl_4$ and 0.10 mM cysteine, under potential cycles between 0 V to −0.8 V for 3000 s.

Published on 27 January 2016. Downloaded by Synchrotron Radiation Library on 23/11/2016 03:11:24.

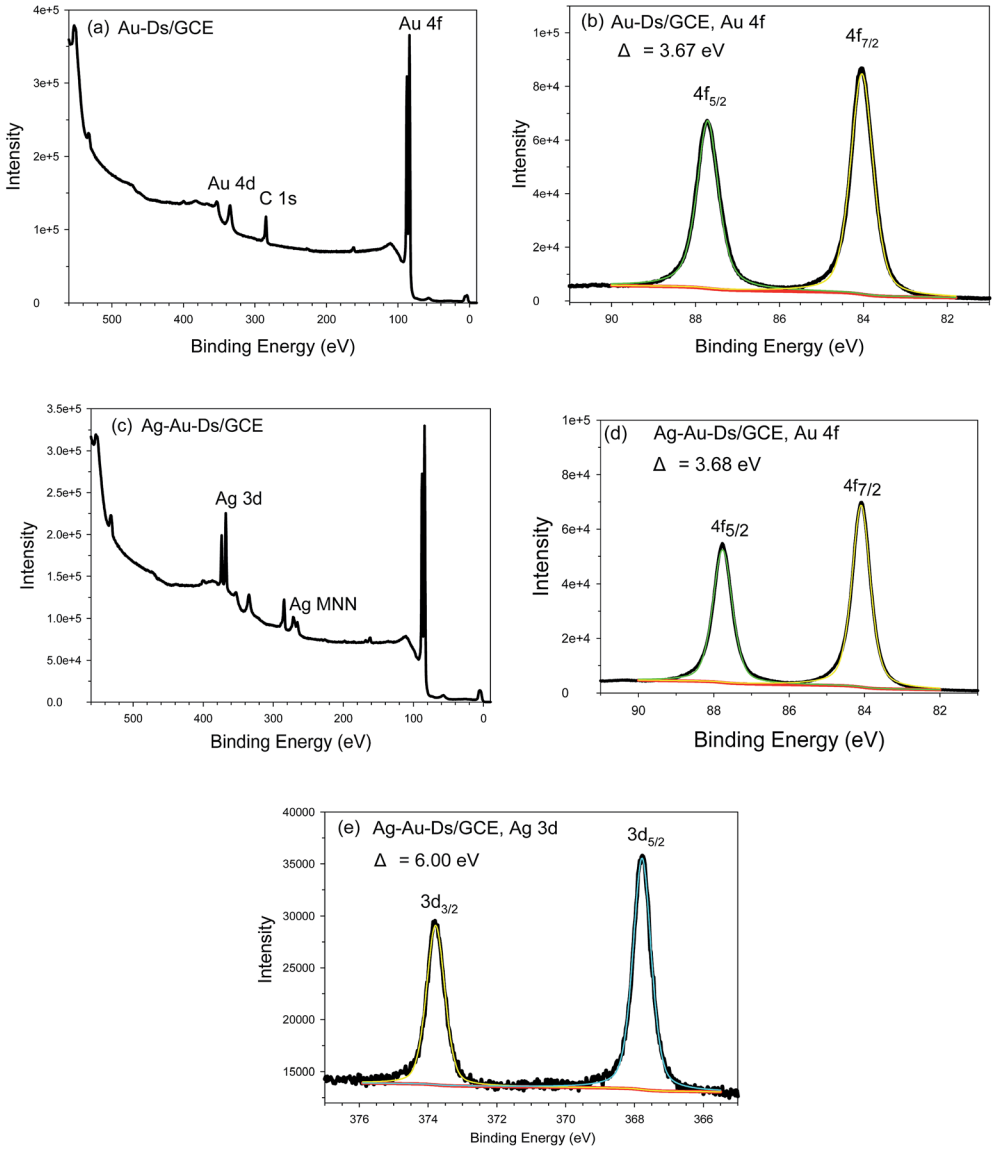

Fig. 2 (a) XPS spectrum of the Au-Ds/GCE and (b) the corresponding fine scan near the Au 4f energy level. (c) XPS spectrum for Ag–Au-Ds/GCE and the corresponding fine scans near the energy levels of (d) Au 4f or (e) Ag 3d.

which may be attributed to the attachment of cysteine to Au crystal surfaces that limited the crystal growth to the ⟨111⟩ direction during the electrodeposition, as that reported previously.[19,30] Moreover, the PXRD pattern of the Ag–Au-Ds in Fig. 3(b) shows no crystalline peaks of Ag. Overall, the SEM, XPS, and PXRD results together suggest that the Ag–Au-Ds comprise hyperbranched crystalline nanostructures of Au-Ds with the surfaces covered with monolayers or sub-monolayers of Ag.

For comparison of SERS effects, the surface areas of Ag–Au-Ds and Au-Ds were deduced respectively from the corresponding cyclic voltammetry (CV) scan profiles measured (Fig. 4). The corresponding ESA was estimated by calculation of the amount of charge consumed during the reduction of the Au surface oxide monolayers, on the basis of the cathodic peak current at *ca.* 0.79 V.[31,32] The hence deduced ESA of Au-D/GCE is *ca.* 6.0 m^2 g^{-1}, based on a scaling constant $S = 400$ μC cm^{-2}, as detailed in ESI.† This corresponds to a molecular adsorption area available for 32 nmol of *p*-NTP, given 1 mg of the gold dendrite Au-Ds. On the basis of the chronocoulometry of the UPD of Ag on Au-Ds/GCE (Fig. S2†), a modified S value of 334 μC cm^{-2} was deduced for the Ag–Au-Ds (with electrode polarization for 200 s). The reduced S value corresponds to *ca.* 50% coverage of Ag on the Au-Ds surfaces, according a linear scaling to the S value of 222 μC cm^{-2} measured for a complete monolayer of Ag on Au surface.[24]

Shown in Fig. 5(a)–(c) are the SERS spectra for *p*-NTP absorbed on Au-Ds/GCE measured at excitation wavelengths of 532, 633, and 785 nm, respectively. Commonly observed in these spectra with different laser excitations is the dependence of SERS intensities on the solution *p*-NTP concentration used in soaking the Au-Ds/GCE and Ag–Au-Ds/GCE samples. These SERS spectra are characterized by three major, prominent

 This journal is © The Royal Society of Chemistry 2016

Published on 27 January 2016. Downloaded by Synchrotron Radiation Library on 23/11/2016 03:11:24.

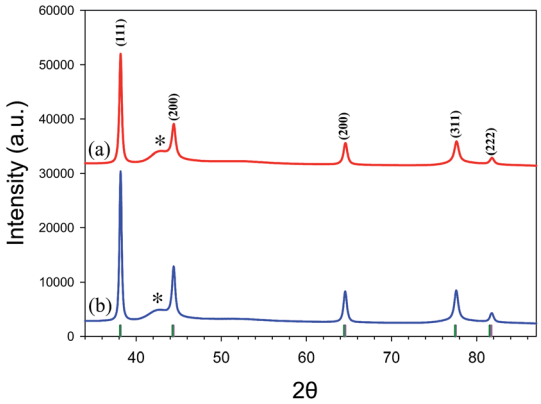

Fig. 3 PXRD patterns of the (a) Au-Ds/GCE and (b) Au–Ag-Ds/GCE. Peaks marked by an asterisk (*) are contributed by the GCE substrate. Diffraction peaks are indexed according to the typical fcc structure of Au crystals.

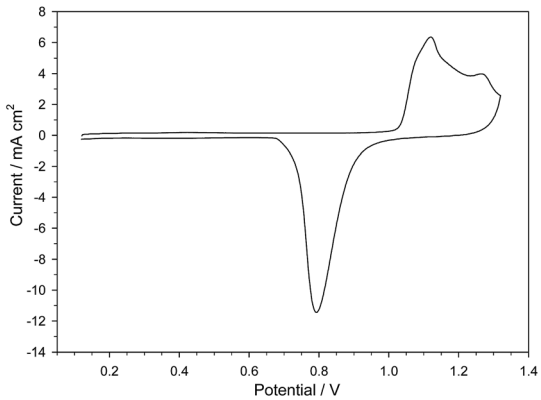

Fig. 4 CV profile recorded at 50 mV s^{-1} for the Au-Ds/GCE in an N_2-saturated solution of 0.05 M H_2SO_4. The GCE area is *ca.* 1 cm^2.

bands at 1078, 1333, and 1571 cm^{-1}, respectively corresponding to the C–S, N–O, and C–C stretching vibrations of *p*-NTP.[28,33,34] The strongest band, $\nu(NO_2)$ is used as a marker for detection limit of *p*-NTP adsorption onto the Au-Ds. In the case of 532 excitation, the *p*-NTP detecting limit with Au-Ds is *ca.* 100 μM. In contrast, the correspondingly measured SERS spectra at 785 nm (Fig. 5(c)) are much enhanced to a lowest *p*-NTP detection limit of 10 nM. Following a previously reported calculation,[6] we estimated the SERS enhancement factor (EF) of the Au dendrites for the SERS bands through the equation

$$\mathrm{EF} = (I_{\text{Au-Ds}}/N_{\text{Au-Ds}})/(I_{\text{ref}}/N_{\text{ref}}) \quad (1)$$

where $I_{\text{Au-Ds}}$ and I_{ref} are the corresponding band intensities of *p*-NTP on Au-D/GC and GCE substrates, respectively normalized by the total number of *p*-NTP molecules of $N_{\text{Au-Ds}}$ and N_{ref}, under the same laser illumination area.[6,28] We note that $N_{\text{Au-Ds}}$ can be deduced based on the solution *p*-NTP concentration, the *p*-NTP–Au binding constant (detailed below) and the ESA of Au-Ds deduced previously. Whereas N_{ref} is deduced from the total amount of *p*-NTP drop cast on the GC substrate. The hence extracted SERS EF values for the 1333 cm^{-1} band of the *p*-NTP/Au-Ds samples are 2.3×10^5, 3.1×10^6, and 1.0×10^7, respectively, under 532, 633, and 785 nm laser excitation. The prominent SERS results evidence the advantages of the densely packed nanostructures of sharp edges and tips of Au-Ds.

To evaluate quantitatively the SERS efficiency of Au-Ds modified by UPD Ag, we also measured parallel SERS spectra (Fig. 5(d) and S1†) with the *p*-NTP absorption on Ag–Au-Ds/GCE. The result reveals comparable SERS effects as that measured for Ag-Ds at 532 and 785 nm laser excitations for a best *p*-NTP detecting limit to 5 nM. However, the SERS intensity measured with 633 nm laser excitation with Ag–Au-D is particularly enhanced by *ca.* three times, compared to that for the parallel measurements with Au-Ds, as shown in Fig. 5(d). The best EF values deduced for 532, 633, and 785 nm excitation, based on the characteristic 1333 cm^{-1} band, are respectively 2.3×10^5, 8.9×10^6, and 9.3×10^6.

Fig. 6 summarizes the SERS EFs of the vibrational band at 1333 cm^{-1} of *p*-NTP adsorption on the Au-Ds/GCE and Ag–Au-Ds/GCE at the three excitation wavelengths. In general, the SERS EF values are increasingly higher with the increase of excitation laser wavelengths. This may be attributed to an increasingly better match of the laser frequency to the ensemble plasmon resonances of the Au-Ds and Ag–Au-Ds of an origin of EM SERS, as suggested previously.[35,36] As the SEM images (Fig. 2) revealed, the dendritic hierarchical structure of Au-DS or Ag–Au-Ds covers a wide range of length scale from nanometers to micrometers, favoring larger structural features with longer wavelength excitation.

As to the case of Ag–Au-DS, the SERS effects involve EM and CM origins.[6] We note that CM enhancement is activated by increased polarizability due to charge transfer between the adsorbed molecules and the SERS substrate. Without blocking the EM SERS from the underneath Au-DS, the Ag monolayers of partial-coverage (*ca.* 50%), however, replace partially the Au/*p*-NTP bonding with Ag-/*p*-NTP bonding interfaces, hence changing the CM enhancement. As a result, the final SERS EF value is contributed by nearly the same EM SERS from the underlying Au-DS, together with an improved CM SERS from the Ag/*p*-NTP bonding (with respect to the Au/*p*-NTP bonding). Our result suggests that at the specific 633 nm laser excitation the CM SERS with the Ag/*p*-NTP bonding together and the molecular architecture of *p*-NTP is particularly advantageous over that with the Au–*p*-NTP bonding, leading to the three times lager SERS enhancement.[11] In contrast, at 532 or 785 nm laser excitations, there are no differences in CM SERS enhancements of the same molecular structure binding onto the Ag– or Au–*p*-NTP surface, leading to similar EF values as illustrated in Fig. 6.

Binding isotherm and binding affinity

In the previous SERS comparison, we have assumed that *p*-NTP binds equivalently to Au-Ds and Ag–Au-Ds *via* thiol–Au or –Ag interactions in solution. On the basis of the *p*-NTP concentration (C_p) dependent SERS intensity *I* (*cf.* Fig. 5), we have further revealed similar *p*-NTP binding affinities, based on the extracted

Published on 27 January 2016. Downloaded by Synchrotron Radiation Library on 23/11/2016 03:11:24.

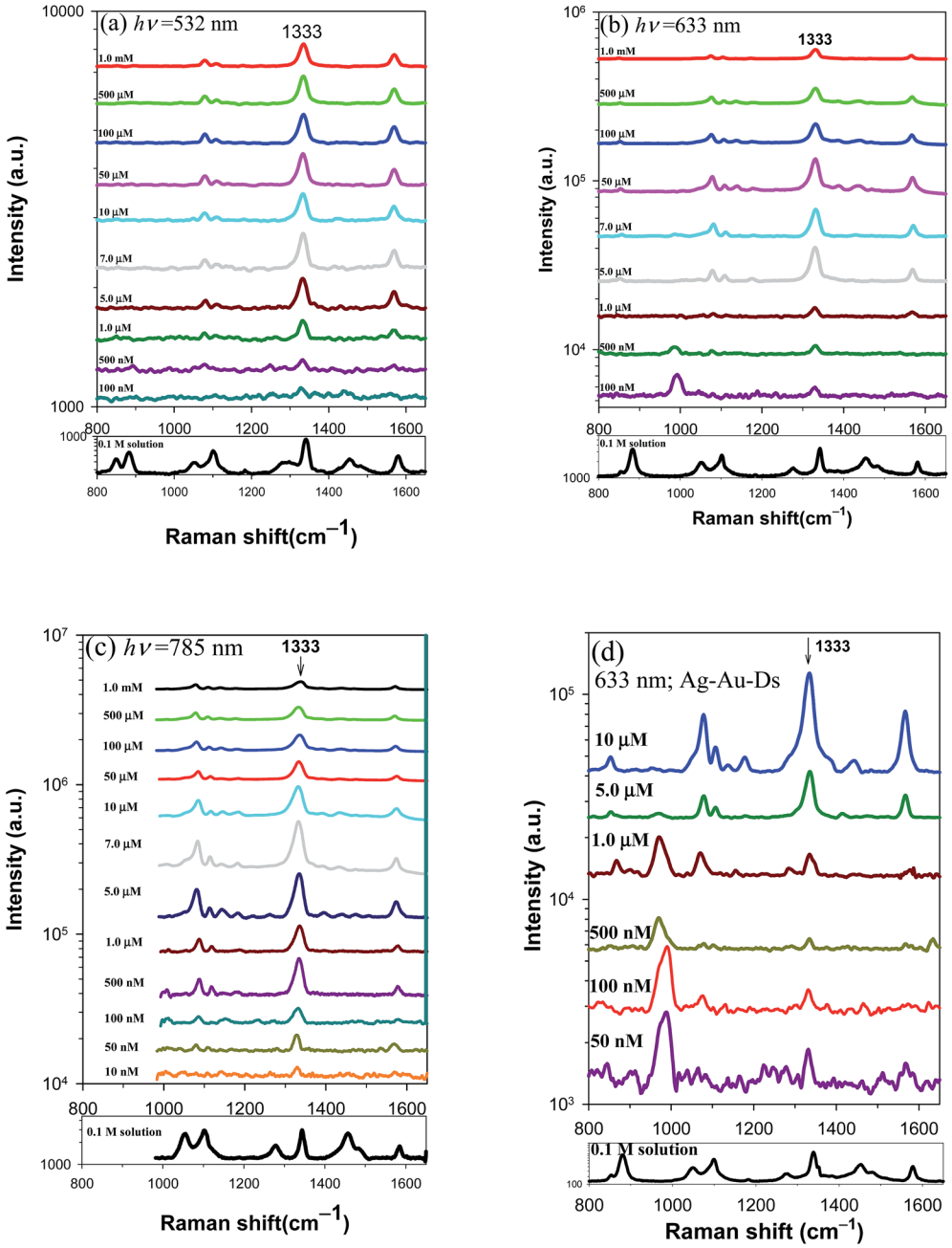

Fig. 5 SERS spectra for the Au-Ds/GCE after immersion in solutions with the indicated *p*-NTP concentrations. The laser excitation wavelengths are (a) 532, (b) 633, and (c) 785 nm. Below are the corresponding spectra for the neat GCE (without Au deposition) drop-coated with a 0.1 M *p*-NTP ethanol solution. (d) The corresponding spectra of *p*-NTP on the Ag–Au-Ds/GCE measured at 633 nm excitation.

surface coverage θ in terms of the Langmuir adsorption isotherm[7]

$$\theta = I/I_0 = \alpha C_p/(1 + \alpha C_p). \quad (2)$$

In the above equation, I_0 is the peak intensity for a saturated *p*-NTP monolayer, and α is the adsorption constant of *p*-NTP adsorbed onto a specific surface. Shown in Fig. 7 are the very similar adsorption isotherms of *p*-NTP to the Au-Ds/GCE and Ag–Au-Ds/GCE substrates, respectively established based on the 1333 cm^{-1} peak intensity in the relevant spectra shown in Fig. 5(b) and (d). Both isotherms can be fitted reasonably well with a common α value $= 100 \pm 30$ mM^{-1} (Fig. 7); correspondingly, a half-coverage concentration $C_{1/2} = 0.01$ mM for 50% coverage of the monolayer can be deduced at $\alpha C_{1/2} = 1$ based on eqn (2). Hence, above $C_{1/2}$ a saturated monolayer of *p*-NTP adsorption on either the substrates can be asymptotically reached, which is consistent with that reported previously.[31] The result of the same or similar α values deduced supports our assumption that *p*-NTP can bind to Ag–Au-Ds and Au-Ds comparably well. The α value also assists the deduction of the

 This journal is © The Royal Society of Chemistry 2016

Published on 27 January 2016. Downloaded by Synchrotron Radiation Library on 23/11/2016 03:11:24.

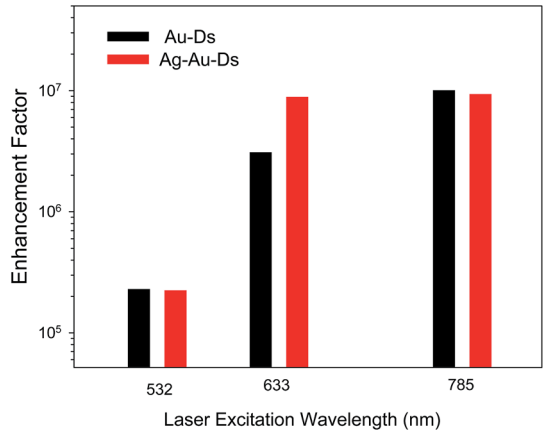

Fig. 6 Excitation-wavelength dependent EF deduced based on the 1333 cm^{-1} band in the SERS spectra of *p*-NTP on the Au-Ds/GCE and Ag–Au-Ds/GCE.

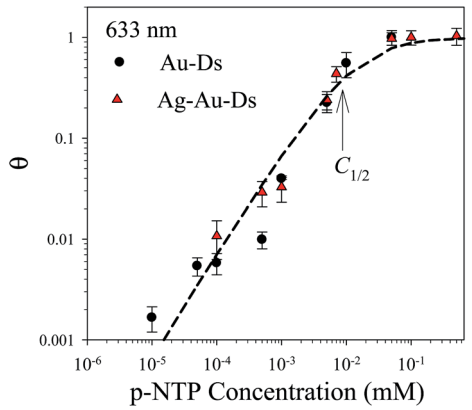

Fig. 7 Binding isotherms for the solution *p*-NTP adsorptions on the Au-Ds/GCE and Ag–Au-Ds/GCE. The isotherms are established based on the 1333 cm^{-1} mode in the SERS spectra measured with 633 laser excitation (shown in Fig. 5), and fitted (dotted curve) using eqn (2).

number of absorbed *p*-NTP on the SERS substrates in solution for obtaining the EF values shown in Fig. 6, according to eqn (1).

Conclusions

In the present study, we have demonstrated the electrochemical fabrication of the efficient SERS substrates Au-Ds/GCE and Au–Ag-Ds/GCE. The cysteine-directed crystalline Au-Ds, of a preferred crystal growth direction along ⟨111⟩, possess a hierarchical architecture comprising trunks, branches, and nanorod-like leaves in a threefold symmetry. After UPD Ag modification, the hierarchical and crystalline structural features of the dendrites remained unaltered. Both Au-Ds and Ag–Au-Ds demonstrate excitation-wavelength dependent SERS for a best detection limit of *p*-NTP in solution down to 10 nM, with 785 nm laser excitation. Particularly, SERS of Ag–Au-Ds outperforms that of Au-Ds at a specific 633 nm laser excitation, and is attributed to improved CM SERS with the Ag–*p*-NTP bonding and the *p*-NTP molecular architecture. A approximately common binding constant extracted from the binding isotherms, established based on the *p*-NTP solution concentration dependent SERS results, suggest similar binding affinities of *p*-NTP to Au-Ds and Ag–Au-Ds.

Acknowledgements

The authors thank Y.-C. Kuo and Dr C.-H. Chen for their assistance with XPS measurements, as well as Dr Y.-C. Lee for the use of the Raman spectrometer. This work was financially supported by the Ministry of Science and Technology (Grant No. NSC 102-2112-M-213-005-MY3).

References

1 C. Costas, V. López-Puente, G. Bodelón, C. González-Bello, J. Pérez-Juste, I. Pastoriza-Santos and L. M. Liz-Marzán, *ACS Nano*, 2015, **9**, 5567–5576.
2 A. Tripathi, E. D. Emmons, A. W. Fountain, J. A. Guicheteau, M. Moskovits and S. D. Christesen, *ACS Nano*, 2015, **9**, 584–593.
3 Y. Wang, B. Yan and L. Chen, *hem. Rev.*, 2013, **113**, 1391–1428.
4 S. Schlücker, *Angew. Chem., Int. Ed.*, 2014, **53**, 4756–4795.
5 P. L. Stiles, J. A. Dieringer, N. C. Shah and R. P. Van Duyne, *Annu. Rev. Anal. Chem.*, 2008, **1**, 601–626.
6 Y.-H. Lai, S.-W. Chen, M. Hayashi, Y.-J. Shiu, C.-C. Huang, W.-T. Chuang, C.-J. Su, H.-C. Jeng, J.-W. Chang, Y.-C. Lee, A.-C. Su, C.-Y. Mou and U. S. Jeng, *Adv. Funct. Mater.*, 2014, **24**, 2544–2552.
7 H. Wang, C. S. Levin and N. J. Halas, *J. Am. Chem. Soc.*, 2005, **127**, 14992–14993.
8 A. La Porta, A. Sanchez-Iglesias, T. Altantzis, S. Bals, M. Grzelczak and L. M. Liz-Marzan, *Nanoscale*, 2015, **7**, 10377–10381.
9 S. L. Kleinman, R. R. Frontiera, A.-I. Henry, J. A. Dieringer and R. P. Van Duyne, *Phys. Chem. Chem. Phys.*, 2013, **15**, 21–36.
10 M. A. El-Sayed, *Acc. Chem. Res.*, 2001, **34**, 257–264.
11 N. G. Tognalli, E. Cortés, A. D. Hernández-Nieves, P. Carro, G. Usaj, C. A. Balseiro, M. E. Vela, R. C. Salvarezza and A. Fainstein, *ACS Nano*, 2011, **5**, 5433–5443.
12 H. Cong, B. Yu, J. Tang, Z. Li and X. Liu, *Chem. Soc. Rev.*, 2013, **42**, 7774–7800.
13 G. Lu, C. Li and G. Shi, *Chem. Mater.*, 2007, **19**, 3433–3440.
14 X. Tang, W. Cai, L. Yang and J. Liu, *Nanoscale*, 2013, **5**, 11193–11199.
15 H. Liu, Z. Yang, L. Meng, Y. Sun, J. Wang, L. Yang, J. Liu and Z. Tian, *J. Am. Chem. Soc.*, 2014, **136**, 5332–5341.
16 X. Bai, Y. Gao and L. Zheng, *CrystEngComm*, 2011, **13**, 3562–3568.
17 S. J. Lee, A. R. Morrill and M. Moskovits, *J. Am. Chem. Soc.*, 2006, **128**, 2200–2201.
18 H. M. Song, L. Deng and N. M. Khashab, *Nanoscale*, 2013, **5**, 4321–4329.
19 T.-H. Lin, C.-W. Lin, H.-H. Liu, J.-T. Sheu and W.-H. Hung, *Chem. Commun.*, 2011, **47**, 2044–2046.

Published on 27 January 2016. Downloaded by Synchrotron Radiation Library on 23/11/2016 03:11:24.

20 Q. Teng, Z. Yongjin, L. Jiaqi, Z. Wenjun, L. Xianzhong, C. Tiejun and K. C. Paul, *J. Phys. D: Appl. Phys.*, 2009, **42**, 175403.
21 K. Jasuja and V. Berry, *ACS Nano*, 2009, **3**, 2358–2366.
22 J. Huang, S. Vongehr, S. Tang, H. Lu, J. Shen and X. Meng, *Langmuir*, 2009, **25**, 11890–11896.
23 Z. Yi, S. Chen, Y. Chen, J. Luo, W. Wu, Y. Yi and Y. Tang, *Thin Solid Films*, 2012, **520**, 2701–2707.
24 C.-C. Chang, K.-H. Yang, Y.-C. Liu, C.-C. Yu and Y.-H. Wu, *Analyst*, 2012, **137**, 4943–4950.
25 Y.-C. Liu, K.-H. Yang and T.-C. Hsu, *J. Raman Spectrosc.*, 2009, **40**, 903–907.
26 H.-S. Sheu, U. S. Jeng, W.-J. Shih, Y.-H. Lai, C.-H. Su, C.-W. Lai, M.-J. Yang, Y.-C. Chen and P.-T. Chou, *J. Phys. Chem. C*, 2008, **112**, 9617–9622.
27 P. Y. Chuang, W. L. Lee, T. F. Teng, Y. H. Lai and W. H. Hung, *J. Phys. Chem. C*, 2009, **113**, 17447–17454.
28 L.-P. Wang, S.-C. Kuo, U. S. Jeng and Y.-H. Lai, *RSC Adv.*, 2015, **5**, 37323–37329.
29 G. K. Jennings and P. E. Laibinis, *J. Am. Chem. Soc.*, 1997, **119**, 5208–5214.
30 Y. Qin, Y. Song, N. Sun, N. Zhao, M. Li and L. Qi, *Chem. Mater.*, 2008, **20**, 3965–3972.
31 S. Xiao, F. Xiao, Y. Hu, S. Yuan, S. Wang, L. Qian and Y. Liu, *Sci. Rep.*, 2014, **4**, 4370.
32 S. Trasatti and O. A. Petrii, *J. Electroanal. Chem.*, 1992, **327**, 353–376.
33 E. M. van Schrojenstein Lantman, T. Deckert-Gaudig, A. J. G. Mank, V. Deckert and B. M. Weckhuysen, *Nat. Nanotechnol.*, 2012, **7**, 583–586.
34 S.-C. Kuo, J.-J. Tasi, J.-S. Li, Z.-H. Hou, C.-H. Li, U.-S. Jeng and Y.-H. Lai, *APL Mater.*, 2014, **2**, 113310.
35 S. M. Adams, S. Campione, J. D. Caldwell, F. J. Bezares, J. C. Culbertson, F. Capolino and R. Ragan, *Small*, 2012, **8**, 2239–2249.
36 Y. Hu, N. Pan, K. Zhang, Z. Wang, H. Hu and X. Wang, *Phys. Status Solidi A*, 2007, **204**, 3398–3404.

This journal is © The Royal Society of Chemistry 2016